Journal of Materials Chemistry A

Accepted Manuscript

This article can be cited before page numbers have been issued, to do this please use: Z. Kan, Z. Wang, Y. Firdaus, M. Babics, H. N. Alshareef and P. Beaujuge, *J. Mater. Chem. A*, 2018, DOI: 10.1039/C8TA02841A.

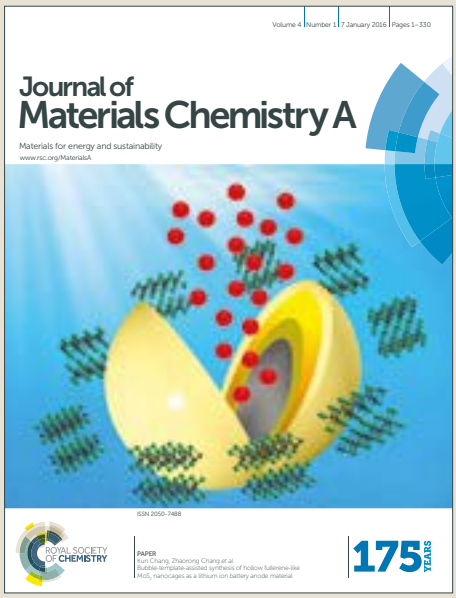

ROYAL SOCIETY OF CHEMISTRY

rsc.li/materials-a

View Article Online
DOI: 10.1039/C8TA02841A

Journal Name

ARTICLE

Atomic-Layer-Deposited AZO Outperforms ITO in High-Efficiency Polymer Solar Cells

Received 00th January 20xx,
Accepted 00th January 20xx

DOI: 10.1039/x0xx00000x

www.rsc.org/

Zhipeng Kan,[1,2,+] Zhenwei Wang,[2,+] Yuliar Firdaus,[1,2] Maxime Babics,[1,2] Husam N. Alshareef,[1,*] and Pierre M. Beaujuge[1,2,*]

Tin-doped indium oxide (ITO) transparent conducting electrodes are widely used across the display industry, and are currently the cornerstone of photovoltaic device developments, taking a substantial share in the manufacturing cost of large-area modules. However, cost and supply considerations are set to limit the extensive use of indium for optoelectronic device applications and, in turn, alternative transparent conducting oxide (TCO) materials are required. In this report, we show that aluminum-doped zinc oxide (AZO) thin films grown by atomic layer deposition (ALD) are sufficiently conductive and transparent to outperform ITO as the cathode in inverted polymer solar cells. Reference polymer solar cells made with atomic-layer-deposited AZO cathodes, PCE10 as the polymer donor and $PC_{71}BM$ as the fullerene acceptor (model systems), reach power conversion efficiencies of *ca.* 10% (compared to *ca.* 9% with ITO-coated glass), without compromising other figures of merit. These ALD-grown AZO electrodes are promising for a wide range of optoelectronic device applications relying on TCOs.

Introduction

Tin-doped indium oxide (ITO) is a composite of indium oxide (In_2O_3) and tin oxide (SnO_2), usually obtained in a 9:1 atomic ratio[1,2]. It is currently widely used in both research laboratories and in the display industry because of its notable optical transparency (as high as 90% transmittance) and low resistivity (commonly up to *ca.* $1.8\times10^{-4}\ \Omega$ cm)[1-3]. Specifically, ITO meets the requirements as electrode material for light emitting displays, thin-film photovoltaics, sensors and photodetectors, and remains a benchmark for optoelectronic device applications in spite of the costs associated with the use of indium in the ternary oxide. The limited natural abundance of indium and its cost are the primary limiting factors driving the research on alternative transparent conductive oxides (TCOs) that could ultimately act as ITO replacements. Of all prospective material candidates for conducting and transparent interlayers, including approaches that rely on carbon nanotubes[4,5], graphene[6,7], silver nanowires[8], and conducting polymers[9,10], metal oxides doped with a ternary element appear to remain the most promising and cost-effective avenue for their concurrently high achievable transparency, conductivity and durability[2,11,12]. Aluminum-doped zinc oxide (AZO) thin films grown by various synthetic methods, such as magnetron sputtering[3,13,14], plasma enhanced chemical vapour deposition,[15] pulsed laser deposition[16], and sol-gel[17] routes commonly meet the transparency and stability requirements; the high sheet resistance of the corresponding films (*ca.* 150 nm; > 75 Ohm/sq) has however lagged behind that of ITO (10 – 15 Ohm/sq). In turn, AZO is currently being used as an interlayer facilitating electron extraction/collection in optoelectronic devices, including polymer solar cells and their hybrid tandem with inorganic photovoltaics, not as a conducting electrode – ITO systematically outperforming AZO in this role.

In recent years, the growth of thin films of oxides by atomic layer deposition (ALD) has become a very effective approach to achieve oxide-based thin-film transistors and p-n junctions with state-of-the-art figures of merit[18-20]. In general, ALD-grown oxide deposition strategies have the benefit of producing (i) conformable, uniform layers over a wide range of substrate types and geometries, (ii) films with very low concentrations of defects compared to other deposition methods, (iii) oxide layers grown at relatively low growth temperatures that are compatible with polymeric flexible substrates. In this contribution, we demonstrate that high-quality AZO thin-film electrodes with high conductivity and transparency can be deposited by ALD at low temperatures. Furthermore, we show that tuning the aluminum dopant concentration, the process temperature, and the thickness of the layers can yield TCO electrodes with work-functions (4.48-4.65 eV) and visible-range transparencies (380-900 nm) comparable to those of sputtered ITO. In polymer solar cells (inverted configuration with PCE10 as the polymer donor and $PC_{71}BM$ as the fullerene acceptor; see **Figure 2**) used as model devices for our demonstration, atomic-layer-deposited AZO cathodes with sheet resistance (R_S) of 16.0 Ohm/sq

Physical Sciences and Engineering Division, [1]Materials Science & Engineering and [2]KAUST Solar Center, King Abdullah University of Science and Technology (KAUST), Thuwal 23955-6900, Saudi Arabia.

Electronic Supplementary Information (ESI) available: [details of any supplementary information available should be included here]. See DOI: 10.1039/x0xx00000x

[+] co-first authors

View Article Online
DOI: 10.1039/C8TA02841A

outperform ITO, and yield higher photocurrents and power conversion efficiencies of *ca.* 10% (compared to *ca.* 9% with ITO-coated glass). Our systematic examinations and comparison of the charge-carrier dynamics, inferred from incident light intensity dependence measurements on the current–voltage (*J–V*) device characteristics, and by transient photovoltage/photocurrent analyses, show that replacing ITO by ALD-grown AZO does not cause further recombination losses at the active layer-electrode interfaces. In parallel, AZO cathodes are found to enhance the photon absorption per volume (G; 1.25×10^{27} $m^{-3}s^{-1}$ for AZO devices vs. 1.00×10^{27} $m^{-3}s^{-1}$ for ITO devices, as will be discussed in later sections), while allowing for better charge generation and extraction, thus explaining the J_{SC} and PCE improvements observed. This work therefore shows that ALD-grown AZO electrodes are promising candidates for a wide range of optoelectronic device applications relying on TCOs.

Results and Discussion

AZO film deposition by ALD

AZO films were deposited on glass substrates following an ALD protocol described in previous work[19]. A schematic of the ALD deposition process is depicted in **Figure S1**. Trimethyl aluminum (TMA), diethyl zinc (DEZ) were used as sources for Al and Zn, and deionized water was used as the oxidant. The AZO film was obtained by the sequential deposition of ZnO and Al_2O_3, which react to form AZO during the growth process. **Figure S1b** shows a schematic of the deposition process of individual Zn-O (DEZ cycle) and Al-O (TMA cycle) layers, while **Figure S1c** illustrates the deposition of multilayers of ZnO and Al_2O_3 to obtain AZO films. The Al doping level can be controlled by adjusting the cycle number of DEZ vs. TMA precursors (DEZ/TMA ratio). In this work, the DEZ/TMA ratios were tuned from 100:0 (neat ZnO film) to 5:1.

AZO film characterizations

In the optimization of AZO film depositions for use as polymer solar cell (PSC) electrodes, a trade-off between the sheet resistance (R_S) and the transmittance of the films must be found. The resistivity (ρ) and R_S of the AZO layers were optimized by taking into account several parameters: DEZ/TMA ratio, growth temperature, and film thickness. **Table S1**, **S2** and **S3** provide the details of our experimental examinations. **Figure 1a** shows the variations of ρ with the DEZ/TMA ratios (established from **Table S1**), and indicate that the lowest ρ value of 1.2×10^{-3} Ohm-cm can be attained at a DEZ/TMA ratio of 20:1 (a film that we henceforth refer to as "20:1 AZO"). The work-function (Φ) values for these AZO films range from 4.48 to 4.65 eV (**Figure 1a** and **Figure S2**). In parallel, **Figure 1b** shows that "20:1 AZO" films yield the highest carrier density (n) value ~4.45×10^{20} cm^{-3}. The n values increase with TMA cycles because additional electrons are introduced in the AZO lattice upon substituting Al^{3+} on the Zn^{2+} lattice site. The n value reaches a maximum then starts to decrease, a behavior that can be attributed to dopant clustering, which has been previously observed[21,22]. **Figure 1b** also indicates that the electron Hall mobility of the films decreases monotonically with increasing numbers of TMA cycles. The changes in carrier concentration and mobility of AZO can be understood with the help of **Figure 1c**. The X-ray diffraction (XRD) shows that the ZnO films are c-axis oriented as indicated by the dominance of the (002) peaks. All peaks shift to higher diffraction angles with decreasing number of DEZ cycles (100 to 5 DEZ cycles), indicating a reduction in the size of the ZnO unit cell. This is probably due to the substitution of smaller ionic radius Al^{3+} (0.39 Å) on Zn^{2+} (0.6 Å). However, further increasing the ratio of TMA/DEZ increases the amount of Al_2O_3 in the film relative to ZnO, and the number of free Al atoms (not bonded to oxygen) that can substitutionally replace Zn. At some point, we may exceed the limit of Al dopant that the ZnO lattice can accommodate.

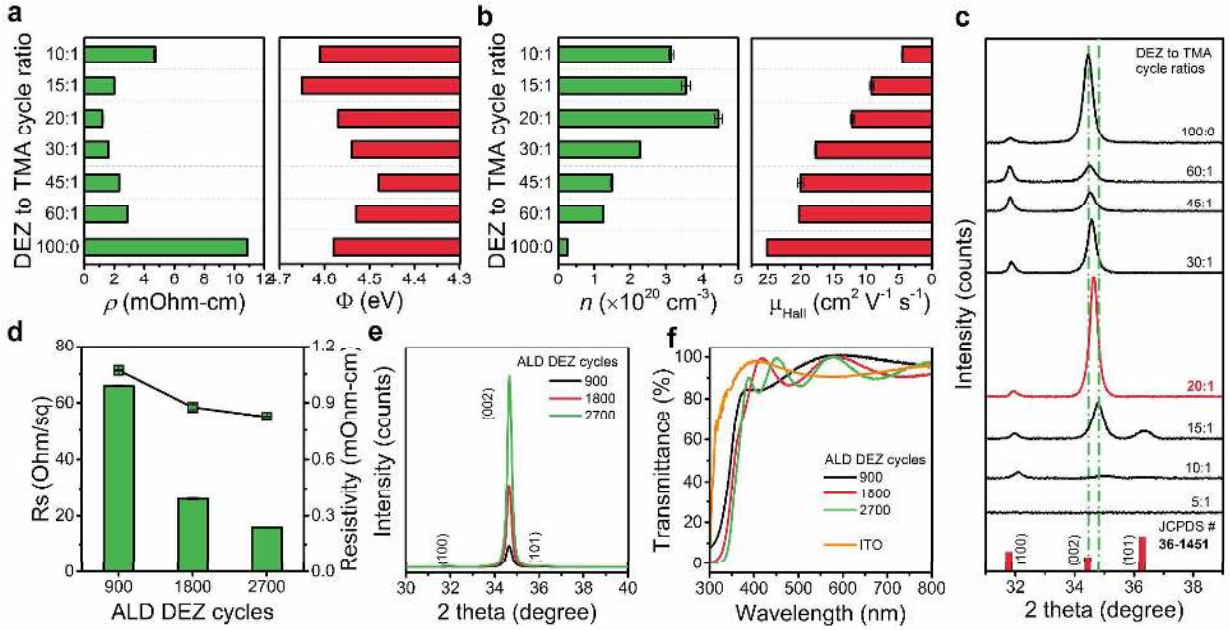

Figure 1 Optimization of AZO films grown by ALD. (a-c) Electronic parameters pertaining to the AZO films formed from various precursor ratios: (a) resistivity & work function; (b) carrier density & Hall mobility; (c) XRD patterns. (d-f) Material properties of the "20:1" AZO films with various thicknesses: (d) sheet resistance & resistivity; (e) XRD patterns; (f) UV-Vis transmittance spectra.

View Article Online
DOI: 10.1039/C8TA02841A

Beyond this limit, Al atoms clustering starts to occur, and the proportion of amorphous Al_2O_3 in the film increases, thereby reducing the crystallinity of the lattice to the point where no characteristic diffraction peaks are observed (amorphous films). **Figure S4** shows that upon Al dopant incorporation, the optical bandgap of ALD-grown AZO films increases, which can be explained by the Burstein-Moss effect[23]. **Figure S5** describes the ALD process temperature optimization, with AZO films grown at 160, 200, and 250 °C (experimental details provided in **Table S2**). The lowest ρ value of 1.1×10^{-3} Ohm-cm is attained for films grown at 200 °C (**Figure S5a**). Interestingly, the AZO layers grown at 160 °C show a (100)-oriented crystal structure, while an evident (101) peak is observed in layers grown at 250 °C, both of which are distinct from the desired c-orientation achieved in AZO films grown at 200 °C (**Figure S5b**). The low ρ value of the layer grown at 200 °C can be correlated to the favorable c-orientation: noting that in-plane electron transport is impeded by scattering centers induced from the arrangement of atoms in the (100)-orientation (layers grown at 160 °C) or from the presence of (101) planes (layers grown at 250 °C). Last, the thickness of the AZO films grown by ALD was optimized to reduce R_S, with the underlying aim of maximizing the open-circuit voltage (V_{OC}; *i.e.* minimizing recombination loss channels at the active layer-electrode interface) and the fill-factor (*FF*) in actual polymer solar cells[24]. From AZO films grown with 900, 1800, and 2700 DEZ cycles (thickness values provided in **Table S3**), the lowest R_S value of 16.0±0.1 Ohm/sq can be achieved for AZO layers grown with 2700 DEZ cycles, corresponding to a ρ value of 8.25×10^{-4} Ohm-cm (**Figure 1d**). All of the AZO films grown under these conditions followed the same favorable c-orientation pattern (**Figure 1e**), along with sufficient transmittance (>88% at 550 nm; similar to ITO) in the visible range (**Figure 1f**). As shown in **Figure S6**, film thickness increased linearly with ALD cycle number, indicating self-limiting film growth. Overall, increasing layer thickness did not affect the work-function, nor did it influence the extent of the optical bandgap (**Figure S6**). The Al composition of the ALD-grown AZO layers obtained from 2700 DEZ cycles was measured to be 3.9 at% by X-ray photoelectron spectroscopy (**Figure S8**). If not otherwise mentioned, AZO electrodes made from the following "optimum" ALD-growth protocol and material characteristics will be used throughout the next sections of this study – deposition: "20:1"AZO / 135 TMA cycles / 2700 DEZ cycles / substrate temperature: 200 °C / AZO thickness: 520 nm / sheet resistance: 16 Ohm/sq.

Fabrication and characterization of polymer solar cells (PSCs)

The AZO electrodes were patterned by wet etching, using diluted HCl as etching reagent ($HCl:H_2O$ = 1.25:100 v/v). The AZO and ITO electrode areas and thicknesses were carefully measured by profilometry prior to the fabrication of PSC devices (**Figure S9**). **Figure 2a** shows the PSC device schematics; device area: 0.1 cm^2, defined by the overlapping Ag and AZO electrodes (delimitated by dashed line). The polymer donor PCE10 and the fullerene acceptor $PC_{71}BM$ were used as model systems for the PSC device fabrication (**Figures 2b** and **2c;** corresponding absorption spectra in **Figure 2d**). PSC devices with an inverted device configuration were adopted for the demonstration; including ZnO[25] as the electron transport layer (ETL), MoO_3 as the hole transport layer (HTL), and Ag as the top electrode (**Figure 2a**). **Figure 2e** provides the schematic energy diagram relative to the PSC device and accounts for each layer in the stack. Reference devices with

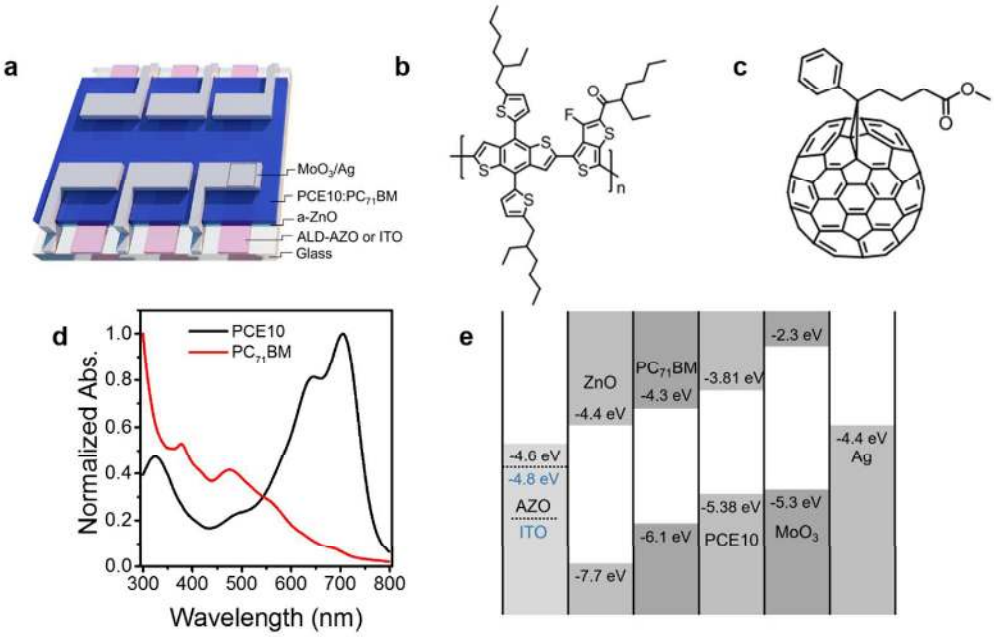

Figure 2 PSC device schematics and energy diagram relative to the PSC devices examined in this study. (a) ITO/AZO electrode pattern and device architecture; (b) chemical structure of the polymer donor PCE10; (c) chemical structure of the fullerene acceptor PC71BM; (d) normalized UV-Vis spectra of PCE10 and PC71BM (thin film); (e) simplified energy diagram representative of the various layers involved in the PSC device stacks.

View Article Online
DOI: 10.1039/C8TA02841A

ITO cathodes and the same PCE10: $PC_{71}BM$ active layer were fabricated for systematic comparison with the AZO-based PSC device counterparts.

The active layers were cast from chlorobenzene (CB), with 3 vol% of 1,8-diiodooctane (DIO), and an optimum donor and acceptor blend ratio of 1:1.5 (wt/wt); optimized protocol described in prior work[26] (cf. details in the Method section; active layer thickness: (avg.) 100 nm). **Figure 3a** shows the *J-V* characteristics of the PSC devices fabricated with either ITO or AZO as the bottom electrodes (cathodes), in the dark and under AM1.5G solar illumination (100 mW cm^{-2}). As shown in **Table 1**, the reference ITO-based PSC devices achieved PCE values of *ca*. 9.2% (*max.* 9.3%), *FF* values of *ca*. 70%, a V_{OC} of *ca*. 0.8 V, and J_{SC} values of *ca*. 16.5 mA cm^{-2} (cf. device statistics in **Table S4**). In comparison, AZO-based PSC devices reached higher PCE values of *ca.* 10.0% (*max.* 10.1%), *FF* values of *ca*. 67%, a V_{OC} of *ca*. 0.8 V, and notably higher J_{SC} values of *ca*. 18.7 mA cm^{-2}. The external quantum efficiency (EQE) spectra of the corresponding devices are compared in **Figure 3d**, noting that the agreement between integrated EQE and J_{SC} values inferred from the *J-V* characteristics (± 0.8 mA cm^{-2}; ±5%) was consistent in comparing ITO- and AZO-based PSC devices. **Figure 3b** confirms that the *J-V* characteristics of AZO-based PSC devices overlap upon forward and reverse biases, reflecting the absence of hysteresis. **Figure 3c** shows that the *J-V* characteristics of AZO-based PSC devices remain unchanged with illumination time, indicating that "light-soaking" effects[27] do not affect device operation. Often times, light-soaking effects arise from the presence of residual oxygen introduced in the ETL deposition step (e.g. TiO_x[28] and polyelectrolytes[29]).

The broad photoresponses from 300 nm to *ca.* 800 nm depicted in **Figure 3d** point to three notable differences between the EQE spectra of ITO- and AZO-based PSC devices: (i) in the wavelength range 300-380 nm, ITO-based devices have a more effective EQE footprint than AZO-based PSCs, as AZO layers possess more parasitic absorption in the UV (**Figure 1f**); (ii) in the range 420-565 nm, AZO-based devices show more prominent interference features and a more effective EQE response than ITO-based PSCs; (iii) in the range 640-730 nm, the EQE spectrum of AZO-based devices peak to *ca*. 83%, representing a 10% increase over that of ITO-based PSCs (detailed in later sections). It is however worth noting that the non-negligible UV absorption of AZO layers below 400 nm filters off wavelengths that are typically considered as potentially damaging to the active layer in PSCs. Light propagation and interference patterns in PSC devices can be examined by optical simulations using transfer matrix modeling (TMM) approaches; the refractive index *n* and extinction coefficient *k* of each layer in the device stack must then be determined from a combination of ellipsometry and UV-Vis spectrometry measurements (using an integrating sphere; cf. experimental details in the SI). **Figures 3e** and **3f** show the simulated depth-profile optical field distribution across the ITO and AZO-based PSC devices, respectively. The variations in optical field distribution across PSC devices typically impact the spectral absorption by the active layer; here, the simulations show that the optical field pattern that reaches the active layers in ITO- and AZO-based devices falls in the wavelength range 350-700 nm. Importantly, the

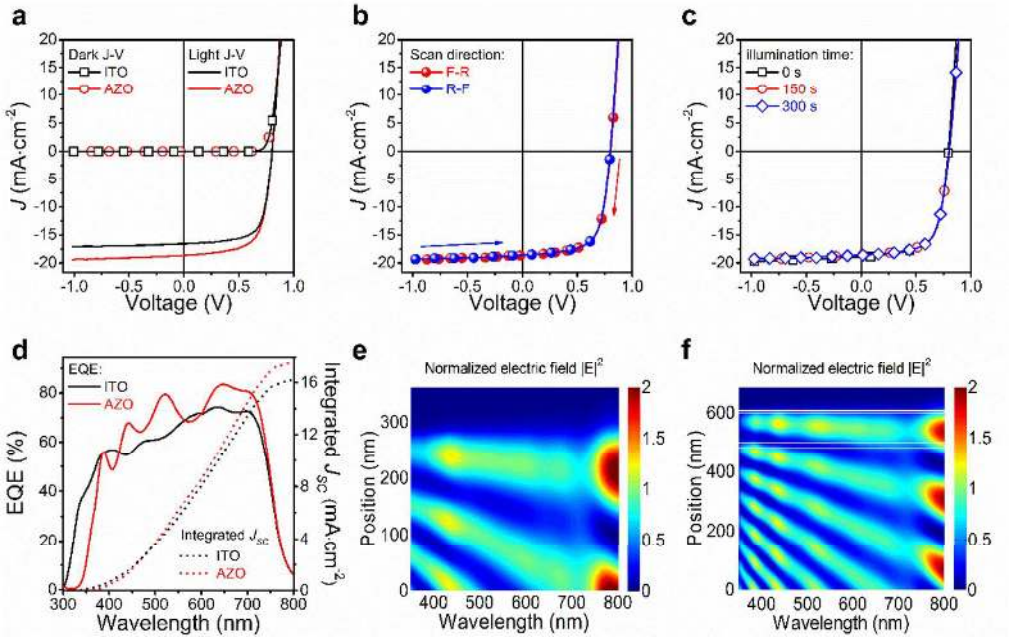

Figure 3 J-V and EQE characteristics of ITO- and AZO-based PSCs. (a) J-V curves under illumination and in the dark; (b) J-V of AZO-based devices with reverse-to-forward and forward-to-reverse bias scans; (c) J-V of AZO-based devices subjected to various illumination times, prior to bias scan; (d) EQE and integrated JSC for the ITO- and AZO-based devices; (e) simulated optical field inside ITO-based devices; (f) simulated optical field across AZO-based PSC devices.

View Article Online
DOI: 10.1039/C8TA02841A

Table 1 PV Performance of the Model PSC Devices, with PCE10 as the Polymer Donor and PC71BM as the Fullerene Acceptor, and with ALD-grown AZO or ITO as the Cathode [a,b].

Cathode	Resistivity Ω/sq	V_{OC} (V)	J_{SC} (mAcm^{-2})	FF (%)	Avg. PCE (%)
ITO	13	0.8	16.5	70	9.2
AZO	16	0.8	18.7	67	10.0

[a] Average values across 10 devices. Device statistics provided in the SI, Table S4

interference pattern in the wavelength range 350-550 nm is more pronounced in AZO-based devices (for optimized AZO films of 520-nm thickness) compared with ITO-based devices (for optimized ITO films of 130-nm thickness) because of the difference in optical spacing width between ITO and AZO layers (cf. additional simulation data for ITO- and AZO-based PSC devices with different electrode layer thicknesses in the SI, **Figure S10**). Further, we note that the more pronounced interference pattern in AZO-based PSCs coincides with the stronger interference features observed in the EQE of the device in the range 420-565 nm (**Figure 3f**). The maximum theoretical J_{SC} of ITO and AZO-based devices can also be inferred from TM modeling, thus taking into account the interference patterns shown in **Figures 3e** and **3f**. From these simulations, the maximum J_{SC} of ITO- and AZO-based devices are predicted to be of comparable magnitude (19.9 and 19.2 mA/cm^2 for ITO and AZO, respectively), suggesting that the higher experimental J_{SC} observed for AZO-based PSCs does not stem from differences in interference effects. Further examinations are required to explain the J_{SC} increase observed in AZO-based devices (detailed in the next section).

Carrier dynamics and extraction in the PSCs

Device performance, the absence of hysteresis and "light-soaking" effect, and optical interference patterns across the AZO- and ITO-based PSC devices were detailed in prior sections. We now turn to the examination of the carrier recombination patterns in the PSC devices. To this end, we performed incident light intensity dependence measurements, considering both the variations in *J-V* characteristics and in transient photocurrent upon illumination. **Figure 4a** and **4b** provide the *J-V* characteristics as a function of incident light intensity for ITO- and AZO-based devices, respectively, and allow for a systematic look at the variations in J_{SC} and V_{OC} with light intensity. A power law dependence of J_{SC} on incident light intensity (I) prevails in PSC devices and can be described as $J_{SC} \propto I^{\alpha}$ based on prior studies[30-32]. The power factor α equal to 1 is indicative of efficient carrier extraction prior to their recombination under short circuit condition. In **Figure 4c**, the dependence of J_{SC} on light intensity is plotted in a log-log scale and fitted to a power law (solid lines). In both ITO- and AZO-based devices, the fitted power factor α is estimated as *ca.* 0.99, indicating that charge carriers are efficiently extracted across both device configurations. In parallel, **Figure 4d** shows the variation of V_{OC} vs. light intensity in a natural log scale,

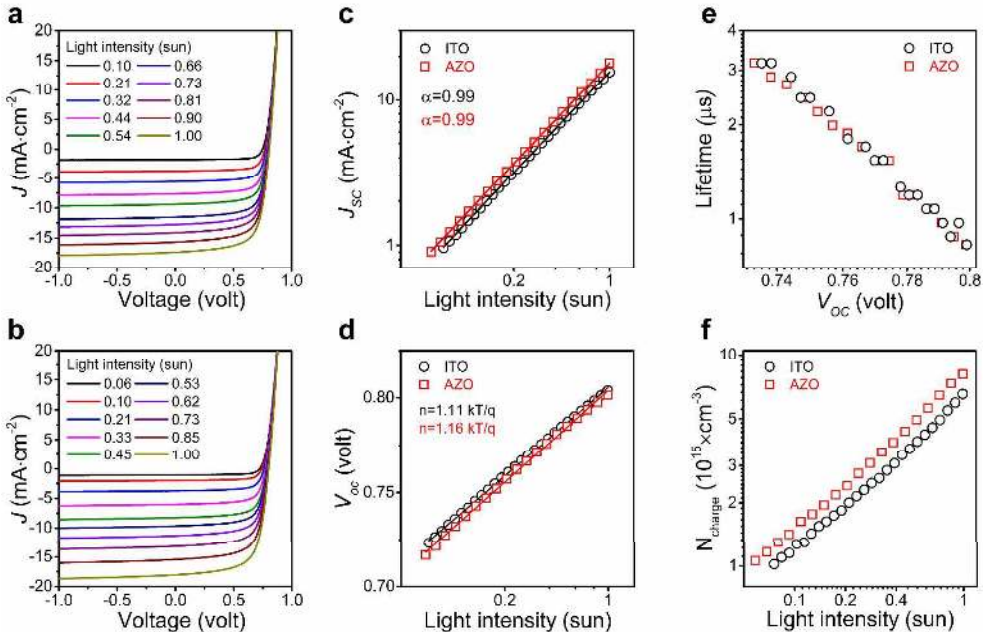

Figure 4 Light intensity dependence J-V and transient photocurrent (TPC) characteristics. Incident light intensity dependence of J-V for (a) ITO-based devices and (b) AZO-based devices; (c) JSC vs. light intensity characteristics for ITO- and AZO-based devices (solid lines are the fits to the experimental data); (d) VOC vs. light intensity characteristics for ITO- and AZO-based devices (solid lines are the fits to the experimental data); (e) carrier lifetime as a function of VOC; (f) charge density extracted from TPC measurements. Symbol legend: ITO-based devices (○) and AZO-based devices (□).

View Article Online
DOI: 10.1039/C8TA02841A

with data fitted to $V_{oc} \propto n\frac{kT}{q}\ln(I)$, where k, T, and q are the Boltzmann constant, temperature in Kelvin, and the elementary charge, respectively. The parameter n (usually in the range of 1 to 2) reflects the presence/absence of carrier traps across the active layers or at interfaces with the electrodes[32]. Any deviations from n = 1 (trap-free condition) point to the existence of recombination effects and, more specifically, to the existence of trap-assisted recombination. As emphasized in **Figure 4d**, n = 1.11 and 1.16 were inferred from our analyses of the ITO- and AZO-based devices, respectively, implying that both devices are subject to some extent of trap-assisted recombination at open circuit. Transient photovoltage measurements can provide further details on the recombination effects occurring in PSCs; here, carrier lifetimes can be inferred from the analysis of the voltage decay induced by small light perturbations[33] (*cf.* experimental details in the SI). **Figure 4e** provide the carrier lifetime estimates as a function of V_{OC} for optimized ITO- and AZO-based PSC devices. As expected, the carrier lifetime of both device configurations is comparable at all V_{OC} and, at 1 sun condition (V_{OC} = 0.8 V), carrier lifetimes of 0.89 µs are estimated in both cases. These observations and estimates, including the comparable recombination patterns under short-circuit and open-circuit conditions, indicate that the carrier recombination dynamics are equivalent across the ITO- and AZO-based PSC devices. In other words, replacing ITO by ALD-grown AZO electrodes does not cause further recombination losses at the active layer-electrode interfaces under short circuit and open circuit conditions.

Considering the similar recombination patterns observed in ITO- and AZO-based PSC devices, the notable photocurrent increase described earlier for AZO-based PSCs may stem from differences in charge generation and/or extraction. To probe this assumption, we estimated the photon flux densities absorbed by the PSC devices per unit volume[30,34] G, assuming that all photogenerated excitons dissociate and contribute to the current generation in the current-saturated regime. The photogenerated current density J_{ph} (*cf.* shown in SI **Figure S11**) can be described by $J_{ph} = qLGP_c$, where q is the elementary charge, L is the thickness of the active layer, and P_C is the charge collection probability. With the assumption stated above, P_C = 1, and the value of G is then described as $G_{max} = \frac{J_{ph.sat.}}{qL}$. The G_{max} and $J_{ph.sat.}$ estimated for the AZO-based device are: *ca.* 1.25×10^{27} $m^{-3}s^{-1}$ and 19.9 mA cm^{-2}, respectively; values that are larger than those for the reference ITO-based device: *ca.* 1.00×10^{27} $m^{-3}s^{-1}$ and 16.7 mA cm^{-2}, respectively. It is worth noting that the G calculated may deviate from the G integrated from optical simulation which can be resulted from the non-unity internal quantum efficiency and charge losses via charge extraction and collection.

As shown in **Figure 2e**, the work function of ZnO, AZO and ITO are -4.4 eV, -4.6 eV, and -4.8 eV, respectively. We also attribute the increase of the photocurrent to the favorable energy alignment of ZnO and AZO, leading to better charge extraction in the AZO-based device than that of ITO-based devices[35]. Carriers extraction across PSC devices can be examined by transient photocurrent (TPC) measurements; here, we examined the turn-on and turn-off dynamics of the ITO- and AZO-based PSCs using long light pulse excitations (200 µs; cf. experimental details in the method section and SI), allowing the currents to reach the steady-state condition. We then calculated the densities of extracted charges by integrating the photocurrent curves at each incident light intensity (after the pulses are turned off); the results are provided in **Figure 4f**. As expected, the density of charges extracted from the AZO-based device was greater than that from ITO-based devices at all light intensities (**Figure 4f**). At 1 sun, the charge density of 8.1×10^{15} cm^{-3} inferred from AZO-based PSCs scales higher than the value of 6.5×10^{15} cm^{-3} for the reference ITO-based devices. Especially, when we compared the normalized TPC at 1 sun condition presented in SI **Figure S13**, we found that the AZO-based PSCs showed higher current in the time resolved current decay till ca. 220

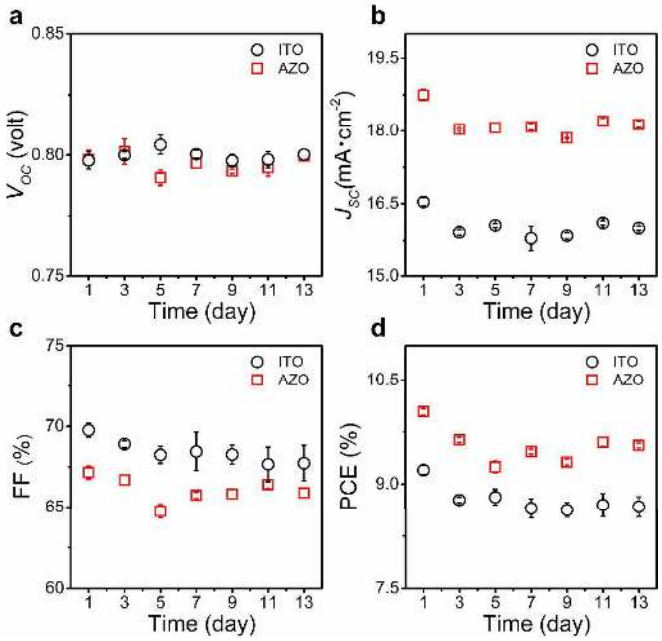

6 | Figure 5 Stability of ITO- and AZO-based PSC devices. Variations of (a) VOC, (b) JSC, (c) FF, and (d) PCE as a function of storage time (in the dark, nitrogen-filled glovebox) of ITO-based devices (○) and AZO-based devices (□).

View Article Online
DOI: 10.1039/C8TA02841A

µs, and then the two devices have same current decay, indicating the AZO based device had better charge extraction compared with that of the ITO based device. In summary, AZO- and ITO-based PSC devices have near-identical recombination patterns, but the AZO-based device is able to absorb greater photon densities, leading to larger charge generation yields, while charge carriers are being effectively collected.

PSC device stability examination

To evaluate and compare the stability of the fabricated AZO- and ITO-based PSC devices, we followed the variations of device performance over a two-week period (devices stored in the N_2-filled glovebox, in the dark; *J-V* measurements performed every other day). As demonstrated in **Figure 5**, the devices underwent only negligible V_{OC} and J_{SC} variations, while both devices underwent comparable *FF* reductions with time. Overall, the AZO-based PSC devices retained PCE values of 9.4% (8.7% for the reference ITO-based devices) over the time of our experiments, demonstrating that the ALD-grown AZO electrodes can effectively replace their (sputtered) ITO counterparts in high-efficiency PSCs, and that the new interface of AZO/ZnO does not cause extra degradation of the PSC devices. Based on our examinations, the limited reduction in device *FF* values observed with time may solely stem from loss channels occurring within the photoactive layer (*e.g.* increased geminate recombination, photobleaching in the presence of residual oxygen, morphological instabilities[36]), as opposed to losses pertaining to the electrodes.

Conclusions

In summary, we have shown that ALD-grown AZO cathodes can outperform ITO in inverted polymer solar cells, yielding higher photocurrents and PCEs of *ca.* 10% (compared to *ca.* 9% for ITO-based devices). Tuning the aluminum dopant concentration, the substrate temperature during the ALD-growth process, and the electrode layer thickness (via number of ALD cycles) results in TCO electrodes with work-functions (4.48-4.65 eV), visible-range transparencies (380-900 nm, >88% at 550 nm), and sheet resistances (16 Ohm/sq) comparable to those of sputtered ITO. Further, using (i) systematic examinations and comparison of the charge-carrier dynamics inferred from incident light intensity dependence measurements on *J–V* device characteristics and (ii) transient photovoltage/photocurrent analyses, we showed that replacing ITO by ALD-grown AZO does not cause further recombination losses at the active layer-electrode interfaces in high-efficiency PSC devices. Overall, AZO-based PSC devices achieve higher photon absorption per volume than their counterparts that use ITO (G; 1.25×10^{27} $m^{-3}s^{-1}$ for AZO devices vs. 1.00×10^{27} $m^{-3}s^{-1}$ for the reference ITO devices) and possess favorable charge generation and extraction patterns – notable characteristics that translate into higher device J_{SC} and PCEs. Our findings suggest that ALD-grown AZO electrodes are useful for a wide range of optoelectronic device applications that require TCOs.

Conflicts of interest

There are no conflicts to declare.

Acknowledgements

Research reported in this publication was supported by King Abdullah University of Science and Technology (KAUST). The authors acknowledge financial support under Baseline Research Funding from King Abdullah University of Science and Technology (KAUST). The authors thank Mohamed N. Hedhili, for his excellent support in the XPS analysis.

Notes and references

1. S. W. Jan and S. C. Lee, *J. Electrochem. Soc.*, 1987, **134**, 6.
2. D. S. Hecht, L. Hu and G. Irvin, *Adv. Mater.*, 2011, **23**, 1482-1513.
3. R. Bel Hadj Tahar, T. Ban, Y. Ohya and Y. Takahashi, *J. Appl. Phys.*, 1998, **83**, 2631-2645.
4. M. W. Rowell, M. A. Topinka, M. D. McGehee, H.-J. Prall, G. Dennler, N. S. Sariciftci, L. Hu and G. Gruner, *Appl. Phys. Lett.*, 2006, **88**, 233506.
5. S. Kim, J. Yim, X. Wang, D. D. C. Bradley, S. Lee and J. C. deMello, *Adv. Funct. Mater.*, 2010, **20**, 2310-2316.
6. J. Wu, H. A. Becerril, Z. Bao, Z. Liu, Y. Chen and P. Peumans, *Appl. Phys. Lett.*, 2008, **92**, 263302.
7. L. Gomez De Arco, Y. Zhang, C. W. Schlenker, K. Ryu, M. E. Thompson and C. Zhou, *ACS Nano*, 2010, **4**, 2865-2873.
8. D.-S. Leem, A. Edwards, M. Faist, J. Nelson, D. D. C. Bradley and J. C. de Mello, *Adv. Mater.*, 2011, **23**, 4371-4375.
9. S.-I. Na, S.-S. Kim, J. Jo and D.-Y. Kim, *Adv. Mater.*, 2008, **20**, 4061-4067.
10. Y. H. Kim, C. Sachse, M. L. Machala, C. May, L. Müller-Meskamp and K. Leo, *Adv. Funct. Mater.*, 2011, **21**, 1076-1081.
11. A. Kumar and C. Zhou, *ACS Nano*, 2010, **4**, 4.
12. Z. Peng, Y. Xia, F. Gao, K. Xiong, Z. Hu, D. I. James, J. Chen, E. Wang and L. Hou, *J. Mater. Chem.*, 2015, **3**, 18365-18371.
13. K. Schulze, B. Maennig, K. Leo, Y. Tomita, C. May, J. Hüpkes, E. Brier, E. Reinold and P. Bäuerle, *Appl. Phys. Lett.*, 2007, **91**, 073521.
14. J.-H. Park, K.-J. Ahn, K.-I. Park, S.-I. Na and H.-K. Kim, *J. Phys. D: Appl. Phys.*, 2010, **43**, 115101.
15. M. D. Barankin, E. Gonzalez Ii, A. M. Ladwig and R. F. Hicks, *Sol. Energy Mater. Sol. Cells*, 2007, **91**, 924-930.
16. M. Y. Lin, S. H. Wu, L. J. Hsiao, W. Budiawan, K. M. Boopathi, W. C. Tu, Y. C. Chang and C. W. Chu, *Opt. Express*, 2016, **24**, 17910-17915.
17. K. Daoudi, B. Canut, M. G. Blanchin, C. S. Sandu, V. S. Teodorescu and J. A. Roger, *Mater. Sci. Eng., C*, 2002, **21**, 5.
18. D. Chen, C. Zhang, Z. Wang, J. Zhang, S. Tang, W. Wei, L. Sun and Y. Hao, *Appl. Phys. Lett.*, 2014, **104**, 243301.
19. P. K. Nayak, Z. Wang and H. N. Alshareef, *Adv. Mater.*, 2016, **28**, 7736-7744.
20. H. Cheun, C. Fuentes-Hernandez, J. Shim, Y. Fang, Y. Cai, H.

View Article Online
DOI: 10.1039/C8TA02841A

Li, A. K. Sigdel, J. Meyer, J. Maibach, A. Dindar, Y. Zhou, J. J. Berry, J. L. Bredas, A. Kahn, K. H. Sandhage and B. Kippelen, *Adv. Funct. Mater.*, 2012, **22**, 1531-1538.
21. D.-J. Lee, H.-M. Kim, J.-Y. Kwon, H. Choi, S.-H. Kim and K.-B. Kim, *Adv. Funct. Mater.*, 2011, **21**, 448-455.
22. J. W. Elam and S. M. George, *Chem. Mater.*, 2003, **15**, 1020-1028.
23. C.-H. Zhai, R.-J. Zhang, X. Chen, Y.-X. Zheng, S.-Y. Wang, J. Liu, N. Dai and L.-Y. Chen, *Nanoscale Res. Lett.*, 2016, **11**, 407.
24. J. D. Servaites, M. A. Ratner and T. J. Marks, *Energy Environ. Sci.*, 2011, **4**, 4410-4422.
25. L. K. Jagadamma, M. Abdelsamie, A. El Labban, E. Aresu, G. O. Ngongang Ndjawa, D. H. Anjum, D. Cha, P. M. Beaujuge and A. Amassian, *J. Mater. Chem. A*, 2014, **2**, 13321-13331.
26. S. Zhang, L. Ye, W. Zhao, D. Liu, H. Yao and J. Hou, *Macromolecules*, 2014, **47**, 4653-4659.
27. C.-Y. Nam, *J. Phys. Chem. C*, 2014, **118**, 27219-27225.
28. J. Kim, G. Kim, Y. Choi, J. Lee, S. H. Park and K. Lee, *J. Appl. Phys.*, 2012, **111**, 114511.
29. W. Xu, R. Xia, T. Ye, L. Zhao, Z. Kan, Y. Mei, C. Yan, X.-W. Zhang, W.-Y. Lai, P. E. Keivanidis and W. Huang, *Adv. Sci.*, 2016, **3**, 1500245-n/a.
30. S. R. Cowan, A. Roy and A. J. Heeger, *Phys. Rev. B*, 2010, **82**.
31. L. J. Koster, M. Kemerink, M. M. Wienk, K. Maturova and R. A. Janssen, *Adv. Mater.*, 2011, **23**, 1670-1674.
32. A. K. K. Kyaw, D. H. Wang, V. Gupta, W. L. Leong, L. Ke, G. C. Bazan and A. J. Heeger, *ACS Nano*, 2013, **7**, 4569-4577.
33. Z. Li, F. Gao, N. C. Greenham and C. R. McNeill, *Adv. Funct. Mater.*, 2011, **21**, 1419-1431.
34. K. Zhang, B. Fan, R. Xia, X. Liu, Z. Hu, H. Gu, S. Liu, H. L. Yip, L. Ying, F. Huang and Y. Cao, *Adv. Energy Mater.*, **0**, 1703180.
35. Z. Peng, Y. Zhang, Y. Xia, K. Xiong, C. Cai, L. Xia, Z. Hu, K. Zhang, F. Huang and L. Hou, *J. Mater. Chem.*, 2015, **3**, 20500-20507.
36. M. Jørgensen, K. Norrman, S. A. Gevorgyan, T. Tromholt, B. Andreasen and F. C. Krebs, *Adv. Mater.*, 2012, **24**, 580-612.

View Article Online
DOI: 10.1039/C8TA02841A

Graphical Abstract:

Aluminum doped zinc oxide electrode grown by atomic layer deposition for polymer

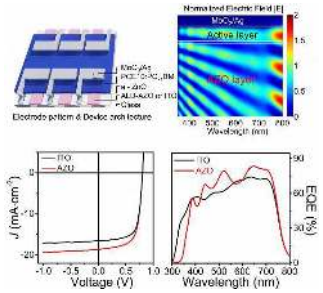

solar cells outperforms ITO in high performance PSC.